The Cryosphere Discuss., 5, 2991–3024, 2011
www.the-cryosphere-discuss.net/5/2991/2011/
doi:10.5194/tcd-5-2991-2011

The Cryosphere Discussions

Melt ponds on Arctic sea ice determined from MODIS satellite data using an artificial neural network

A. Rösel[1,2], **L. Kaleschke**[1], **and G. Birnbaum**[3]

[1]Institute of Oceanography, University of Hamburg, Bundesstr. 53, 20146 Hamburg, Germany
[2]Max Planck Institute for Comparative and International Private Law, Mittelweg 187, 20148 Hamburg, Germany
[3]Alfred Wegener Institute for Polar and Marine Research, Am Handelshafen 12, 27570 Bremerhaven, Germany

Received: 26 September 2011 – Accepted: 3 October 2011 – Published: 27 October 2011

Correspondence to: A. Rösel (anja.roesel@zmaw.de)

Published by Copernicus Publications on behalf of the European Geosciences Union.

Abstract

Melt ponds on sea ice strongly reduce the surface albedo and accelerate the decay of Arctic sea ice. Due to different spectral properties of snow, ice, and water, the fractional coverage of these distinct surface types can be derived from multispectral sensors like MODIS using a spectral unmixing algorithm. The unmixing was implemented using a multilayer perceptron (MLP) to reduce computational costs.

Arctic-wide melt pond fractions and sea ice concentrations are derived from the level 3 MODIS surface reflectance product. The validation of the MODIS melt pond data set was conducted with aerial photos from the MELTEX campaign 2008 in the Beaufort Sea, data sets from the National Snow and Ice Data Center (NSIDC) for 2000 and 2001 from four sites spread over the entire Arctic, and with ship observations from the trans-Arctic HOTRAX cruise in 2005. The root-mean-square errors (RMSE) range from 3.8 % for the comparison with HOTRAX data, over 10.7 % for the comparison with NSIDC data, to 10.3 % and 11.4 % for the comparison with MELTEX data, with correlations coefficients ranging from $R^2 = 0.28$ to $R^2 = 0.45$. The mean annual cycle of the melt pond fraction for the entire Arctic shows a strong increase in June, reaching a maximum of 15 % by the end of June. The zonal mean of melt pond fractions indicates a dependence of the temporal development of melt ponds from the geographical latitude, and has its maximum in mid-July in latitudes between 80° and 88° N.

Furthermore, the MODIS results are used to estimate the influence of melt ponds on retrievals of sea ice concentrations from passive microwave data. Results from a case study comparing sea ice concentrations from ASI-, NASA Team 2-, and Bootstrap-algorithms with MODIS sea ice concentrations indicate an underestimation of around 40 % for sea ice concentrations retrieved with microwave algorithms.

TCD
5, 2991–3024, 2011

1 Introduction

In boreal summer, melt ponds are a common feature on Arctic sea ice and they can cover up to 50 to 60 % of the sea ice area (Fetterer and Untersteiner, 1998; Eicken et al., 2004). On a flat topography of first-year ice and in an early melt stage the melt pond fraction can even rise up to 90 % (Perovich et al., 2011a). Melting caused by shortwave insolation and surface air temperatures above the freezing point during summer results in the development of melt ponds on the sea ice surface and a decrease of the surface albedo from approximately 0.8 to 0.5 which excites additional heat uptake (Curry et al., 1995; Perovich and Tucker, 1997). The appearance of melt ponds has a significant influence on Earth's radiation balance (Maslanik et al., 2007; Perovich et al., 2007; Nicolaus et al., 2010) and therefore also an impact on the strength of the ice-albedo feedback (Tschudi et al., 2008). In order to better constrain the role of sea ice for the Arctic amplification and Earth's climate system, it is important to quantify the large-scale distribution of melt ponds (e.g., Holland et al., 2006; Eisenman and Wettlaufer, 2009; Notz, 2009; Tietsche et al., 2011; Serreze, 2011; Serreze et al., 2011; Kurtz et al., 2011; Perovich et al., 2011b).

Several field experiments and ship observations took place on different locations of the Arctic ocean to study albedo and spectral behavior of melt ponds (Morassutti and LeDrew, 1996; Perovich et al., 2002a), as well as distribution and size of the ponds (El Naggar et al., 1995; Perovich et al., 2002b, 2009; Sankelo et al., 2010; Nicolaus et al., 2010).

Although the potential of different spectral behavior of ponded sea ice in comparison to bare or snow-covered sea ice for satellite applications was proposed already by Grenfell in 1977, the first implementations were published 20 years later by Tschudi et al. (1997, 2001, 2008); Markus et al. (2003) and Rösel and Kaleschke (2011). All studies until now show only by example that melt pond determination from different satellite data is possible. But to our knowledge, there is neither an Arctic-wide nor a multiannual melt pond data set existing.

TCD
5, 2991–3024, 2011

Many spectral and total albedo values for various surface types are given in the literature (e.g., Grenfell and Maykut, 1977; Grenfell and Perovich, 1984; Warren, 1982; Perovich, 1996; Perovich et al., 2002a; Brandt et al., 2005). The values range from 0.06 for open water over 0.29 for mature melt ponds to 0.87 for new snow.

The date of melt onset is related to the amount of solar energy absorbed by the surface (Perovich et al., 2007). Therefore, a zonal onset of the first melt processes is observable, starting in mid-April in the southern Arctic regions like Bering Sea and Hudson Bay. In the Central Arctic, first melting starts in June (Markus et al., 2009). In mid-June, a significant fraction of sea ice is already covered by melt ponds (Perovich et al., 2007).

Melt pond development starts with the melting of snow. Melt water of snow and ice is collecting in surface depressions and other deformated structures. Compared to the much more irregular surface topography of multi-year ice, the plane and flat surfaces of first-year ice have the potential to host large and extended melt pond areas (Fetterer and Untersteiner, 1998).

As melting develops, pond water drains through porous ice and cracks. Yackel et al. (2000) also describe the pond behavior and distribution on multi-year ice as smaller, deeper, and more numerous than on first-year ice.

The heat transmission of water exceeds the one of ice, therefore the melt rate beneath ponds is 2–3 times that of bare ice (Untersteiner, 1979). Therefore the ponds deepen and can even melt through the ice layer. With the increasing depth of the ponds, the diameter of the ponds decreases (Fetterer and Untersteiner, 1998).

Melt ponds are nearly salt free and the density maximum of the ponded water lies well above the freezing point. This means that radiative heating favors convection within the pond: the warmer water will sink down and causes further melting. Convection and mixing of the water is further influenced by wind (Fetterer and Untersteiner, 1998).

Freeze-up starts in late August or early September, caused by low air temperatures, and melt pond fraction decreases. The start of snowfall after the freeze-up will cover

TCD
5, 2991–3024, 2011

the melt ponds and the albedo of the surface rises.

This study is based on a retrieval method for the melt pond fraction from Moderate Resolution Image Spectroradiometer (MODIS) data, founded on spectral unmixing into different surface fractions, published by Tschudi et al. (2005, 2008). We implement an additional constraint to obtain surface fractions in the range between zero and one and use an artificial neural network (ANN) to speed up the processing of large MODIS data sets.

The overall goal of this study is to quantify the surface fractions for melt ponds, open water, and snow and ice for the entire Arctic region for a time period from 2000–2011.

This paper is structured as followed: first, a characterization of the MODIS data used in this study and the data handling is given; additionally, the data used for validation are presented. This is followed by a description of the method of retrieving the melt pond fraction and the sea ice concentration. This includes the generation of a training and a test data set as well as the neural network set-up. Subsequently, validation studies are presented. The last chapter gives a discussion and conclusion.

2 Data

The collection of the MODIS sensor "Terra" beginning from the end of the year 1999, and the additional sensor "Aqua", starting its acquisitions from 2002 until now, results in a complete spatial observation of the Arctic sea ice over the last twelve melting cycles. MODIS measures in 36 spectral bands, ranging from 0.4 µm to 14.4 µm with a resolution from 250 m to 1 km.

We use the MOD09A1 weekly surface reflectance data product with a spatial resolution of 500 m to retrieve the MODIS melt pond fraction. Effects of atmospheric scattering and absorption are corrected in the MOD09 products. Additionally, a correction of the bidirectional reflectance distribution function (BRDF) is applied (Vermonte et al., 2008). For the validation studies we use the MOD09GA daily surface reflectance product.

TCD
5, 2991–3024, 2011

For the analysis of the data we reproject the original MODIS tiles into a polar stereographic projection, mosaic them, and apply a cloud-mask as well as a land-mask, both of which are contained in the MOD09 product. For the comparison with the validation data, we generate true color composites using the spectral band combination 2-4-3 of the MODIS level 1B product.

For validation we use the results of of the melt pond observations from the HOTRAX 2005 cruise (Perovich et al., 2009), the melt pond data set from the National Snow and Ice Data Center (NSIDC) (Fetterer et al., 2008), and the results of the aircraft campaign MELTEX ("Impact of melt ponds on energy and momentum fluxes between atmosphere and sea ice") conducted by the Alfred Wegener Institute for Polar and Marine Research (AWI) in May and June 2008 over the Beaufort Sea (Birnbaum et al., 2009) (see Fig. 1).

The MELTEX campaign aimed to improve the quantitative understanding of the impact of melt ponds on radiation, heat, and momentum fluxes over Arctic sea ice. For this purpose, the BASLER BT-67 type aircraft POLAR 5 was employed, which had a downward-looking digital photo camera aboard. Weather conditions in May were mainly characterized by cold-air advection from the inner parts of the Arctic towards the coast of the Southern Beaufort Sea. These cold air flows caused a refreezing of most melt ponds, which were still very shallow at that time. Even a thin layer of fresh snow on the refrozen ponds was observed. During the last week of measurements in the beginning of June, a tongue of very warm air was shifted from Alaska to the Beaufort Sea. It reached its largest extension over the ocean on 4 and 5 June 2008, which strongly forced the development of melt ponds.

Aerial photography was carried out with a digital SLR camera and a lens with a diagonal angle of view of 114°. A photo was taken every 6 s. In the preprocessing, all photos with sunglint were eliminated, and a cross-track illumination correction was carried out. Subsequently, a supervised classification employing the maximum likelihood method was performed to derive the aerial fraction of the five surface classes distinguished: open water, thin ice, bare ice, snow, and melt ponds. Training data was manually defined in the photos. The probability threshold for the classification was set

TCD
5, 2991–3024, 2011

to 0.95. Pixels, which fell below this threshold were not classified. Only images with a number of unclassified pixels below 5 % were included in the present study. Because of the very shallow and partly refrozen ponds, the determination of melt pond fraction based on an analysis of the aerial photos is difficult for days earlier than 4 June 2008. In the present study, we therefore use only photos from two flights performed on 4 and 7 June 2008 for validation. The flight level of the aircraft determines the surface area covered by the photos. At 1000 m, a photo covers an area of 1.4×2.0 km, and at 30 m, a photo covers an area of 40×60 m. For further comparison the melt pond set is filtered by a Gaussian filter with sigma = 10 to smooth the function, then we pick every tenth value to avoid oversampling.

Sea ice melt pond statistics and maps over four Arctic ocean sites during the summers of 1999, 2000, and 2001, derived from visible band imagery from high resolution satellite data with a spatial resolution of 1 m, are mapped from $10 \times 10\,\mathrm{km}^2$ satellite scenes (Fetterer et al., 2008). These data sets were analyzed using a supervised maximum likelihood classification to derive either two (water and ice) or three (water, ice, and melt ponds) surface classes (Fetterer et al., 2008). The resulting melt pond data set consists of tables of pond coverage and size statistics for $500 \times 500\,\mathrm{m}^2$ cells. Therefore, the spatial resolution of the melt pond set matches to the resolution of the MODIS data set. For the comparison with the MODIS melt pond data, we select only the specific days where MODIS data are available and compare them to the mean of the corresponding high resolution grid cells of one $10 \times 10\,\mathrm{km}^2$ satellite scene. Locations of the three sites (i) Beaufort Sea, (ii) north of the Canadian Archipelago, and (iii) Fram Strait are indicated in Fig. 1.

The results of the melt pond observations from the HOTRAX 2005 cruise (Perovich et al., 2009) are also used for validation. The HOTRAX 05 cruise track was a trans-Arctic journey, entering the pack ice on 9 August 2005 at 74° N, 160° W and traveling in the ice until its exit on 27 September 2005 at 77° N, 9° E. The expedition crossed the Bering, Chukchi, and Beaufort Seas, passed the North Pole on 12 September 2005 and exited the Arctic basin through Fram Strait (see Fig. 1). During the cruise, observations

TCD
5, 2991–3024, 2011

from the bridge of sea ice concentration, melt pond fraction, and ice thickness were conducted on an hourly basis and daily mean values were calculated (Perovich et al., 2009). For this study we use only the melt pond observations.

3 Methodology

The spectral albedo of sea ice is a function of the wavelength of incident solar radiation (see Fig. 2). Highest albedo values appear in short wavelength range from 400–600 nm for dry snow. The albedo is decreasing toward longer wavelengths. At 500 nm melt ponds have albedo values that range between 0.6 for young and shallow ponds and 0.25 for mature ponds. The albedo values for melt ponds depend on the depth and underlying surface of the ponds.

Snow-covered ice, bare ice, wet snow, and melting bare ice, show a smaller reduction in spectral albedo at higher wavelengths than the different types of melt ponds. The albedo of ponded ice is characterized by a decrease between 500 nm and 800 nm. In this wavelength range the absorption of water becomes a dominant factor, which causes the reduction of the spectral albedo. Above 800 nm radiation is nearly totally absorbed by the water surface and the underlying ice layer has no influence on the albedo (Grenfell and Maykut, 1977). The spectral curve for open water (Fig. 2h) shows values around 0.06 though the entire spectrum.

Based on the differences of the spectral curves in Fig. 2, we decide to distinguish in this study between three surface types: open water (W), melt ponds (M), and snow and ice (I) (Tschudi et al., 2008; Rösel and Kaleschke, 2011).

To calculate the albedo of sea ice on a large scale, the surface-based albedo values are weighted with the fraction of their corresponding surface component (Fetterer and Untersteiner, 1998; Tschudi et al., 2008; Perovich et al., 2009).

The so-called areally averaged albedo $\overline{\alpha}$ for larger areas containing three surface types is expressed as

$$\overline{\alpha} = \alpha_W A_W + \alpha_M A_M + \alpha_I A_I \quad (1)$$

TCD
5, 2991–3024, 2011

where A is the area fraction, α is the wavelength-integrated albedo and the indexes W, M, I stand for the surface types open water, melt ponds, and snow and ice, respectively.

The determination of three surface types on Arctic sea ice is based upon a spectral unmixing procedure of satellite images and proposed by Tschudi (2005, 2008).

It relies on the following equations:

$$\begin{aligned} A_W r_W(\lambda_1) + A_M r_M(\lambda_1) + A_I r_I(\lambda_1) &= R(\lambda_1) \\ A_W r_W(\lambda_3) + A_M r_M(\lambda_3) + A_I r_I(\lambda_3) &= R(\lambda_3) \\ A_W r_W(\lambda_4) + A_M r_M(\lambda_4) + A_I r_I(\lambda_4) &= R(\lambda_4) \\ A_W + A_M + A_I &= 1 \end{aligned} \quad (2)$$

where $R(\lambda_k)$ is the reflectance of each band $k = 1$, 3, and 4, with the corresponding wavelengths $r(\lambda_1) = 459$–475 nm, $r(\lambda_3) = 620$–670 nm, and $r(\lambda_4) = 841$–876 nm, for each MODIS pixel. A is the fractional coverage of each surface type in a gridcell, for each band, and $r(\lambda_k)$ represents the spectral reflectance for each surface type. The specific reflectance values for the three surface types used for these equations are listed in Table 1.

The sea ice concentration A_C is quantified as:

$$A_c = 1 - A_w \text{ and } A_c > 15\ \% \quad (3)$$

With the assumption of a three class mixture model and the selection of three surface types, we assure that the set of linear equations (2) is well-posed (see Fig. 2).

To comply with the physical principles, it is necessary to constrain the interval of the solution between zero and one for each class. This is done by a sigmoid function, implemented as cost function F_{cost}:

$$F_{cost} = [(\boldsymbol{r} \cdot \boldsymbol{x}) - \boldsymbol{R}] + [1 - (\tanh(\boldsymbol{x}\gamma) - \tanh((\boldsymbol{x} - 1)\gamma))]w \quad (4)$$

where $\boldsymbol{r}$ is the vector of the spectral reflectance values for each surface type, $\boldsymbol{x}$ is a vector of initial guess values for the fractions of surface types, $\boldsymbol{R}$ is the vector of the

TCD
5, 2991–3024, 2011

measured reflectance values ($\boldsymbol{R} = [R(\lambda_1), R(\lambda_3), R(\lambda_4)]^T$), γ is a gradient to define the slope of the function at the values zero and one, and w is a weighting factor. In our function we choose $\boldsymbol{x} = [0.25, 0.25, 0.25]^T$, $\gamma = 150$, and $w = 0.1$. The results do not depend on the choice of $\boldsymbol{x}, \gamma$, and w; the processing is stable.

Thus, we consider the linear equations (Eq. 2) together with the side condition as an optimization problem. The solution of this problem using the Broyden-Fletcher-Goldfarb-Shanno (BFGS) method causes higher computational costs as compared to the solution of the linear equations (Eq. 2) alone.

To speed up processing, we use an artificial neural network (ANN). With the open source package FFNET for Python (Wojciechowski, 2011) we build a feed-forward multilayer perceptron (MLP), composed of an input layer, two hidden layers with 9 neurons in the first and 27 neurons in the second layer, and one output layer (see Fig. 3). In this case the number of neurons of the input layer is equal number of neurons of the output layer. For our purposes the MLP was trained with back-propagation as learning technique with 5000 learning steps (see e.g., Atkinson and Tatnall, 1997). The amount of layers, neurons and learning steps was determined by following the trial-and-error approach.

To train the ANN, an existing data set of melt ponds needs to be provided as the training data set: We obtain this training data set by solving the equations (Eq. 2) including the above described constraints for a limited amount of pixels from different surface types and different dates. The achieved surface fractions for open water, snow and ice, and melt ponds are used to train the ANN.

To asses the consistence and the accuracy of the ANN we perform two tests: for the first test the training data set is used as test data set. For the second test, independent test data sets are selected. The results of the performance regarding consistence and accuracy of the ANN are presented in the following chapter.

TCD
5, 2991–3024, 2011

4 Results

4.1 Accuracy of ANN

To test the consistence of the ANN, we first apply the trained ANN on the selected training data set and compare the results with the results calculated with the unmixing algorithm.

Thereafter we operate the ANN on eight completely independent test data sets regarding date and region and compare the results as well with the results determined with the unmixing algorithm. The difference between the two methods is for the first case 0.1 %, and for the second case less than 1 %.

For estimation of the methodical error of this procedure, we perform two further tests on the following assumptions:

- An area of $50 \times 50\,\mathrm{km}^2$ around the coordinates 61.5° N and 26.0° W (Denmark Strait, SW of Iceland) is an open water area in June.
- Melting has not started on day 129 of the year 2008 in a latitude of 82.5° N (Markus et al., 2009). An area of $200 \times 100\,\mathrm{km}^2$ around the coordinates 82.5° N and 92.5° W (Northern Beaufort Sea) is covered with dry snow and/or bare cold ice in the first week of May. No melt ponds are observable.

The test for the open water area results in a relative error of +0.1 % for the estimated melt pond fraction, for the test on the snowy surface the relative error is 6 %.

The fractional coverage of water, ice, melt ponds, and the sea ice concentration is derived for the entire Arctic by using the trained ANN and MOD09 mosaics.

4.2 MODIS melt ponds and sea ice concentration

Figures 4 and 5 show the MODIS melt pond data set and the MODIS sea ice concentration data set for the year 2008, both gridded to 12.5 km. They are displayed here to exemplify the processing of one seasonal cycle. We define a seasonal cycle from the

TCD
5, 2991–3024, 2011

beginning of May (day 129 of the MODIS data set) until the first week of September (day 249 of the MODIS data set). Later in September, when new ice is formed, the melt pond fractions increase in areas of new thin ice.

In Fig. 6 the mean melt pond fraction for the entire Arctic within the annual cycles for the years 2000 to 2011 is illustrated. The mean melt pond fraction has a strong increase in June. By the end of June, the maximum with a mean melt pond fraction above 15 % is reached, followed by a second maximum in end of July.

The zonal mean of the melt ponds for the last 12 years is display in Fig. 7 which demonstrates a dependence of the temporal development of melt ponds from the geographical latitude.

The maximum of the average melt pond fraction is located from mid-June to mid-August between 70° and 80° N. A second maximum is indicated in the lower latitudes (below 65° N) in June which displays the strong initial melting along the coastlines. The decrease of the mean melt pond fraction in the higher latitudes (above 80° N) in August indicates a refreezing of the ponds.

From a case study we demonstrate that we can estimate the influence of melt ponds on the conventional sea ice concentration determination from microwave imagery by comparing them with the calculated MODIS sea ice concentration.

Figure 8 displays in the first three images sea ice concentration from AMSR-E sensor, calculated with the ASI algorithm (Spreen et al., 2008), the NASA-Team 2 (NT2) algorithm (Markus and Cavalieri, 2000), and the Bootstrap (BT) algorithm (Comiso, 1995) for the area of the Canadian Archipelago with values from 50–80 % ice coverage. The fourth image displays MODIS sea ice concentration, whereas sea ice concentration from MODIS indicates values from 90–100 %. In the same area, a high fraction of melt ponds (up to 70 %) is determined (bottom image). The ASI Algorithm gives, for a 250 × 100 km region around the coordinate 72° N and 110° W, a mean sea ice concentration of 45 %; the Bootstrap algorithm gives for the same area 55 % sea ice concentration, and the NASA team 2 algorithm shows a value of 56 %. Compared to the sea ice concentration of 93 % retrieved from the MODIS data, all microwave

TCD
5, 2991–3024, 2011

algorithms underestimate the sea ice concentration by around 40 %.

4.3 Validation

For validation we compare the MELTEX melt pond data with MODIS data for 4 and 7 June 2008 (Figs. 9 and 10). In the true color composite (Figs. 9a and 10a) melt ponds can be determined on the individual ice floes as bluish areas, ranging from light blue to a dark turquoise.

By following the MELTEX flight track in both figures, the changing from medium melt pond fractions (20–25 %) to high melt pond fractions (28 %) is reflected in the underlying MODIS melt pond fractions. The transition to the open water areas is also characterized by a decreasing MODIS melt pond fraction.

The flight on 4 June started only at 18:03 UTC and ended at 00:09 UTC the next day. After comparison of the daily level 2 MODIS data from 4 June with the individual level 1B acquisitions, we conclude that the corresponding area in the MOD09GA product derives from an acquisition in the early morning (04:00 UTC or 06:15 UTC). The same is valid for the MOD09GA product of 5 June. Because of the rapidly changing meteorological conditions on 4 June in combination with the late flight time (18:03 UTC until 00:09 UTC) and the early acquisitions of the MODIS scenes, we used the MODIS melt ponds determined from the scene from 5 June for validation. To fill up the gaps caused by cloud filtering in the MODIS melt pond sets, we use the corresponding pixel from the melt pond sets from days before and after the relevant data (Figs. 9b and 10b).

The average MODIS melt pond fraction for the entire flight tracks are 28.4 % ± 2.5 and 21.6 % ± 8.1 for 4 and 7 June. The corresponding MELTEX melt pond fractions are with 26.4 % ± 11.5 and 19.3 % ± 13.5 slightly lower. The calculated root mean square errors (RMSE) for the dates 4 and 7 June are 11.2 % and 10.6 % accordingly.

Figure 11 shows the comparison of NSIDC melt pond data versus MODIS melt pond data. One part of the data (mainly Beaufort data and one data point from the Canadian site) has a high accordance with the MODIS melt pond data, the other part of the data shows lower values than the MODIS data. The RMSE for the data of all sites and both

TCD
5, 2991–3024, 2011

years amounts 10.7 % with a correlation coefficient $R^2 = 0.28$.

The HOTRAX melt pond observations used for our validation study are daily means with standard deviation. Details of the accuracy of the collected data a not are given in Perovich et al. (2009). In Fig. 12 the observations are plotted versus MODIS melt pond results.

The compared mean values are distributed evenly with a correlation coefficient $R^2 = 0.45$ and a determined RMSE of 3.8 %. The observed differences may result from geolocation errors or time differences between ship observation and satellite acquisition. Additionally, there is no information about the accuracy of the ship observation data.

5 Discussion

The determination of the melt pond fraction of the entire Arctic sea ice over an extended period of time is important to estimate the contribution of the melt ponds on the ice-albedo feedback mechanism. The above described method allows us to derive daily and weekly data sets of the melt pond fraction, as well as for the sea ice concentration from MODIS MOD09 data. We use the daily data sets to validate MODIS melt pond fractions and the weekly data sets for generating the time series for the entire Arctic.

Since the weekly data set is a composition of selected pixel from the daily acquisitions, especially with low cloud cover fraction and other atmospheric influences, this product represents only the conditions of a specific day in one week.

The comparison of MODIS melt pond fractions with aerial photos and sea ice observations from different locations in the Arctic shows good agreement. This demonstrates that the technique to estimate the fraction of melt ponds performs well.

The observed differences between validation data and MODIS data may result from the different spatial resolution, from geolocation errors and/or time differences between observations and satellite acquisition. The validation with the MELTEX data demonstrate that MELTEX data has more variability than the MODIS data – this may result

TCD
5, 2991–3024, 2011

from the relatively coarse resolution of 500 m per MODIS pixel used as the basis for this product compared to the averaged size of melt ponds of about 15–60 m^2 (Perovich et al., 2002b).

Potential sources of errors are to be assumed in the atmospheric correction and the influence of the viewing geometry and the solar angles. The BRDF of the MOD09 product is not performed on all areas of the Arctic sea ice, especially not over the deep ocean, because of the moving sea ice surface. For most of the areas model results for first-year and multi-year ice are used as a priori estimates of the BRDF (personal communication with Crystal Schaaf, NASA). Our assumption of the three-surface-class model also causes uncertainties regarding the different fractions, because in reality the Arctic sea ice cover is a mosaic of various surface types.

Figure 7 shows a zonal increase of the melt pond fraction correlating to the increasing solar elevation and with a maximum of the average melt pond fraction located in the higher latitudes, between 70° and 80° N, although the melt period is shorter in high latitudes. This was also observed by Tschudi et al. (2008) and may be caused by a larger sea ice concentration and a thicker ice coverage, which allows less runoff. Therefore more water is retained to form melt ponds (Tschudi et al., 2008).

The pattern of melt pond distribution in early summer (Fig. 4) with the areas with an increased melt pond fraction in the beginning of June indicates the ice free areas later in September. This agrees with the statements of Perovich et al. (2002b, 2011b), that early occurrence of melt ponds have a strong influence on the formation of open water areas. Clearly visible is also the appearance of homogeneous areas with a very high melt pond fraction up to 70 % at the end of June on the flat first year ice in the Canadian Archipelago. The decrease of melt ponds in the week starting from 28 August 2008 was caused by a cold air advection from Greenland with temperatures far below the freezing point. The weather situation changed on 5 September 2008, as warm continental air masses from Siberia caused further melting in the Siberian Arctic and the Fram Strait.

TCD
5, 2991–3024, 2011

The method described here is based on optical satellite data – therefore melt pond fractions can only be identified from cloud free data. In the autumn results we recognized that the spectral signal of thin ice areas looks similar to the spectral signal of melt ponds. Therefore the algorithm specifies in autumn, when new ice is formed, areas at the sea ice edges where thin ice most likely areas occurs as ponded sea ice. For this reason our melt pond data set ranges from beginning of May (day 129) until the first week of September (day 249).

The multiannual melt pond data set has a variety of potential applications, like the parameterization of melt ponds in climate models, the analysis of the interannual variability as well as the trends of melt processes and their influence in the sea ice-albedo feedback mechanism. Additionally to the melt pond data set, we archive a sea ice concentration data set from MODIS data. This sea ice concentration data set, in combination with the melt pond data set, is a valuable basis for quantifying the error caused by melt features in sea ice concentration data derived from passive microwave imagery. As shown in Fig. 8, the MODIS sea ice concentration product has potential to estimate the influence of melt ponds on the sea ice concentration determination from microwave sensors like AMSR-E. In this example, all AMSR-E algorithms are clearly underestimating the actual sea ice concentration by around 40 %.

6 Conclusions

In this study we present a procedure to generate multiannual melt pond and sea ice concentration data sets for extensive areas from MODIS satellite data as shown exemplary on the melting cycle for the year 2008.

The MODIS surface reflectance values are described by a set of linear equations. By selecting three surface types and using reflectances from three bands, we assure that the linear equations are well-posed. By solving the equations we retrieve three surface fractions: open water, snow and ice, and melt ponds.

TCD
5, 2991–3024, 2011

To constrain the interval of the solution between zero and one, a cost function is introduced. The implementation of this cost function leads to an optimization problem. To accelerate the processing, we use a trained ANN. Testing the performance of the ANN as described in Sect. 4 results in stable results with a maximal error of 6 % for the melt pond product.

The mean melt pond fraction for the entire Arctic derived from MODIS satellite data of the last 12 years shows a strong increase in June. By the end of June the maximum with a mean melt pond fraction above 15 % is reached, followed by a second maximum in end of July.

The zonal mean of the melt ponds is dependent on the temporal development of melt ponds from the geographical latitude. The maximum of the average melt pond fraction is situated in the higher latitudes, between 70° and 80° N.

The retrieved MODIS sea ice concentration shows, that sea ice concentration derived from microwave sensors underestimates the actual sea ice concentration by 40 %.

In this paper we present a method to retrieve for the first time a multiannual data set of melt pond fraction and sea ice concentration derived from MODIS satellite data for the entire Arctic. The developed MODIS melt pond data set and the sea ice concentration data of the last twelve melt cycles provide a profound basis for further studies.

Acknowledgements. We thank Donald K. Perovich from the Cold Regions Research and Engineering Laboratory (CRREL) for providing the HOTRAX melt pond data, and Florence Fetterer from NSIDC for her efforts in providing more melt pond statistics. Wolfgang Dierking, Christof Lüpkes and Jörg Hartmann from the AWI participated in the MELTEX aircraft campaign in 2008 and provided useful information for our study. We also want to mention namely both student workers from AWI, Bruno Schyska and Pascal Schwarz for the analysis of the aerial photos of the MELTEX campaign. Additionally, we thank the scientific editor and the reviewers for their profound comments and suggestions. The work was founded by a scholarship of the International Max-Planck-Research-School for Maritime Affairs in Hamburg. Additional support was provided by the Cluster of Excellence CliSAP (EXC177), University of Hamburg, founded through the German Science Foundation (DFG).

The service charges for this open access publication have been covered by the Max Planck Society.

References

Atkinson, P. M. and Tatnall, A. R. L.: Introduction – neural networks in remote sensing, Int. J. Remote Sens., 18, 699–709, doi:10.1080/014311697218700, 1997. 3000

Birnbaum, G., Dierking, W., Hartmann, J., Lüpkes, C., Ehrlich, A., Garbrecht, T., and Sellmann, M. (Eds.): The Campaign MELTEX with Research Aircraft "POLAR 5" in the Arctic in 2008, Berichte zur Polar- und Meeresforschung/Reports on Polar and Marine Research, 593, 3–85, 2009. 2996

Brandt, R. E., Warren, S. G., Worby, A. P., and Grenfell, T. C.: Surface albedo of the Antarctic sea ice zone, J. Climate, 18, 3606–3622, 2005. 2994

Comiso, J. C.: SSM/I Sea Ice Cioncentrations Using the Bootstrap Algorithm, NASA Reference Publication, 1380, 1–50, 1995. 3002

Curry, J. A., Schramm, J. L., and Ebert, E. E.: Sea ice-albedo climate feedback mechanism, J. Climate, 8, 240–247, 1995. 2993

Eicken, H., Grenfell, T. C., Perovich, D. K., Richter-Menge, J. A., and Frey, K.: Hydraulic controls of summer Arctic pack ice albedo, J. Geophys. Res., 109, C08007, doi:10.1029/2003JC001989, 2004. 2993

Eisenman, I. and Wettlaufer, J. S.: Nonlinear threshold behavior during the loss of Arctic sea ice-albedo, P. Natl. Acad. Sci. USA, 106, 28–32, doi:10.1073/pnas.0806887106, 2009. 2993

El Naggar, S., Garrity, C., and Ramseier, R.: Sea Ice Meltpond Morphology and Size Distribution as Determined from Line Scan Camera Local Measurements in the Arctic, in: IAPSO Proceedings XXI General Assembly, 19, Honolulu, Hawaii, 5–12 August, 1995. 2993

Fetterer, F. and Untersteiner, N.: Observations of melt ponds on Arctic sea ice, J. Geophys. Res., 103, 24821–24835, 1998. 2993, 2994, 2998

Fetterer, F., Wilds, S., and Sloan, J.: Arctic sea ice melt pond statistics and maps, 1999–2001, Digital Media (ftp), http://nsidc.org/data/g02159.html, 2008. 2996, 2997

Grenfell, T. and Maykut, G.: The optical properties of ice and snow in the Arctic Basin, J. Glaciol., 18, 445–463, 1977. 2993, 2994, 2998, 3014

TCD
5, 2991–3024, 2011

Grenfell, T. C. and Perovich, D. K.: Spectral albedos of sea ice and incident solar irradiance in the Southern Beaufort Sea, J. Geophys. Res., 89, 3573–3580, 1984. 2994
Holland, M. M., Bitz, C. M., and Tremblay, B.: Future abrupt reductions in the summer Arctic sea ice, Geophys. Res. Lett., 33, L23503, doi:10.1029/2006GL028024, 2006. 2993
Kurtz, N. T., Markus, T., Farrell, S. L., Worthen, D. L., and Boisvert, L. N.: Observations of recent Arctic sea ice volume loss and its impact on ocean-atmosphere energy exchange and ice production, J. Geophys. Res., 116, C04015, doi:10.1029/2010JC006235, 2011. 2993
Markus, T. and Cavalieri, D. J.: An enhancement of the NASA Team sea ice algorithm, IEEE T. Geosci. Remote, 38(3), 1387–1389, 2000. 3002
Markus, T., Cavalieri, D. J., Tschudi, M. A., and Ivanoff, A.: Comparison of aerial video and Landsat 7 data over ponded sea ice, Remote Sens. Environ., 86, 458–469, doi:10.1016/S0034-4257(03)00124-X, 2003. 2993
Markus, T., Stroeve, J. C., and Miller, J.: Recent changes in Arctic sea ice melt onset, freezeup, and melt season length, J. Geophys. Res.-Oceans, 114, C12024, doi:10.1029/2009JC005436, 2009. 2994
Maslanik, J., Drobot, S., Fowler, C., McPhee, G., Emery, W., and Barry, R.: On the Arctic climate paradox and the continuing role of atmospheric circulation in affecting sea ice conditions, Geophys. Res. Lett., 34, L03711, doi:10.1029/2006GL028269, 2007. 2993
Morassutti, M. P. and LeDrew, E. F.: Albedo and depth of melt ponds on sea-ice, Int. J. Climatol., 16, 817–838, doi:10.1002/(SICI)1097-0088(199607)16:7¡817::AID-JOC44¿3.0.CO;2-5, 1996. 2993
Nicolaus, M., Gerland, S., Hudson, S. R., Hanson, S., Haapala, J., and Perovich, D. K.: Seasonality of spectral albedo and transmittance as observed in the Arctic Transpolar Drift in 2007, J. Geophys. Res., 115, C11011, doi:10.1029/2009JC006074, 2010. 2993
Notz, D.: The future of ice sheets and sea ice: between reversible retreat and unstoppable loss, P. Natl. Acad. Sci. USA, 106, 20590–20595, doi:10.1073/pnas.0902356106, 2009. 2993
Perovich, D. K.: The optical properties of sea ice, CRREL Monograph, 96-1, 25 pp., 1996. 2994
Perovich, D. K. and Tucker, W. B. I.: Arctic sea-ice conditions and distribution of solar radiation during summer, Ann. Glaciol., 25, 445–450, 1997. 2993
Perovich, D. K., Grenfell, T. C., Light, B., and Hobbs, P. V.: Seasonal evolution of the albedo of multiyear Arctic sea ice, J. Geophys. Res., 107, 8044, doi:10.1029/2000JC000438, 2002a. 2993, 2994
Perovich, D. K., Tucker III, W. B., and Ligett, K. A.: Aerial observations of the evolution of ice sur-

TCD
5, 2991–3024, 2011

face conditions during summer, J. Geophys. Res., 107, 8048, doi:10.1029/2000JC000449, 2002b. 2993, 3005
Perovich, D. K., Light, B., Eicken, H., Jones, K. F., Runciman, K., and Nghiem, S. V.: Increasing solar heating of the Arctic Ocean and adjacent seas, 1979–2005: Attribution and role in the ice-albedo feedback, Geophys. Res. Lett., 34, L19505, doi:10.1029/2007GL031480, 2007. 2993, 2994
Perovich, D. K., Grenfell, T. C., Light, B., Elder, B. C., Harbeck, J., Polashenski, C., Tucker III, W. B., and Stelmach, C.: Transpolar observations of the morphological properties of Arctic sea ice-albedo, J. Geophys. Res., 114, C00A04, doi:10.1029/2008JC004892, 2009. 2993, 2996, 2997, 2998, 3004
Perovich, D. K., Jones, K. F., Light, B., Eicken, H., Markus, T., Stroeve, J., and Lindsay, R.: Solar partitioning in a changing Arctic sea-ice cover, Ann. Glaciol., 52(57), 192–196, 2011a. 2993
Perovich, D. K., Richter-Menge, J. A., Jones, K. F., Light, B., Elder, B. C., Polashenski, C., Laroche, D., Markus, T., and Lindsay, R.: Arctic sea-ice melt in 2008 and the role of solar heating, Ann. Glaciol., 52(57), 355–359, 2011b. 2993, 3005
Rösel, A. and Kaleschke, L.: Comparison of different retrieval techniques for melt ponds on Arctic sea ice from Landsat and MODIS satellite data, Ann. Glaciol., 52(57), 185–191, 2011. 2993, 2998
Sankelo, P., Haapala, J., Heiler, I., and Eero, R.: Melt pond formation and temporal evolution at the station Tara during summer 2007, Polar Res., 29, 311–321, doi:10.1111/j.1751-8369.2010.00161.x, 2010. 2993
Serreze, M. C.: Rethinking the sea-ice tipping point, Nature, 471, 47–48, doi:10.1038/471047a, 2011. 2993
Serreze, M. C., Barrett, A. P., and Cassano, J. J.: Circulation and surface controls on the lower tropospheric air temperature field of the Arctic, J. Geophys. Res., 116, D07104, doi:10.1029/2010JD015127, 2011. 2993
Spreen, G., Kaleschke, L., and Heygster, G.: Sea ice remote sensing using AMSR-E 89-GHz channels, J. Geophys. Res., 113, C02S03, doi:10.1029/2005JC003384, 2008. 3002
Tietsche, S., Notz, D., Jungclaus, J. H., and Marotzke, J.: Recovery mechanisms of Arctic summer sea ice, Geophys. Res. Lett., 38, L02707, doi:10.1029/2010GL045698, 2011. 2993
Tschudi, M., Curry, J., and Maslanik, J.: Determination of areal surface-feature coverage in the Beaufort Sea using aircraft video data, Ann. Glaciol., 25, 434–438, 1997. 2993

TCD
5, 2991–3024, 2011

Tschudi, M., Curry, J., and Maslanik, J.: Airborne observations of summertime surface features and their effect on surface albedo during FIRE/SHEBA, J. Geophys. Res., 106, 15335–15344, 2001. 2993

Tschudi, M. A., Maslanik, J. A., and Perovich, D. K.: Melt pond coverage on Arctic sea ice from MODIS, in: Proceeding, Amer. Met. Soc. 8th Conf. on Polar Meteorology and Ocean, San Diego, CA, 8–14 January, 2005. 2995, 2999

Tschudi, M. A., Maslanik, J. A., and Perovich, D. K.: Derivation of melt pond coverage on Arctic sea ice using Modis observation, Remote Sens. Environ., 112, 2605–2614, doi:10.1016/j.rse.2007.12.009, 2008. 2993, 2995, 2998, 2999, 3005, 3012

Untersteiner, N.: Sea ice observations, B. Am. Meteorol. Soc., 60, 846–846, 1979. 2994

Vermonte, E. F., Kotchenova, S. Y., and Ray, J. P.: MODIS Surface Reflectance User's Guide, MODIS Land Surface Reflectance Science Computing Facility, version 1.2 edn., http://modis-sr.ltdri.org/products/MOD09_UserGuide_v1_3.pdf, 2008. 2995

Warren, S. G.: Optical properties of snow, Rew. Geophys. Space Ge., 20, 67–89, 1982. 2994

Wojciechowski, M.: FFNET: Feed-forward neural network for python, available at: http://ffnet.sourceforge.net/, last access: 20 October 2011, 2011. 3000

Yackel, J. J., Barber, D. G., and Hanesiak, J. M.: Melt ponds on sea ice in the Canadian Archipelago: 1. Variability in morphological and radiative properties, J. Geophys. Res., 105(C9), 22049–22060, doi:10.1029/2000JC900076, 2000. 2994

TCD
5, 2991–3024, 2011

Table 1. Spectral reflectances (r_i) of surface types used in the unmixing algorithm (after Tschudi et al., 2008).

MODIS band	bandwidth (nm)	resolution (m)	pond r_i	snow/ice r_i	open water r_i
1	459–479	500	0.22	0.95	0.08
3	620–670	250	0.16	0.95	0.08
4	841–876	250	0.07	0.87	0.08

TCD
5, 2991–3024, 2011

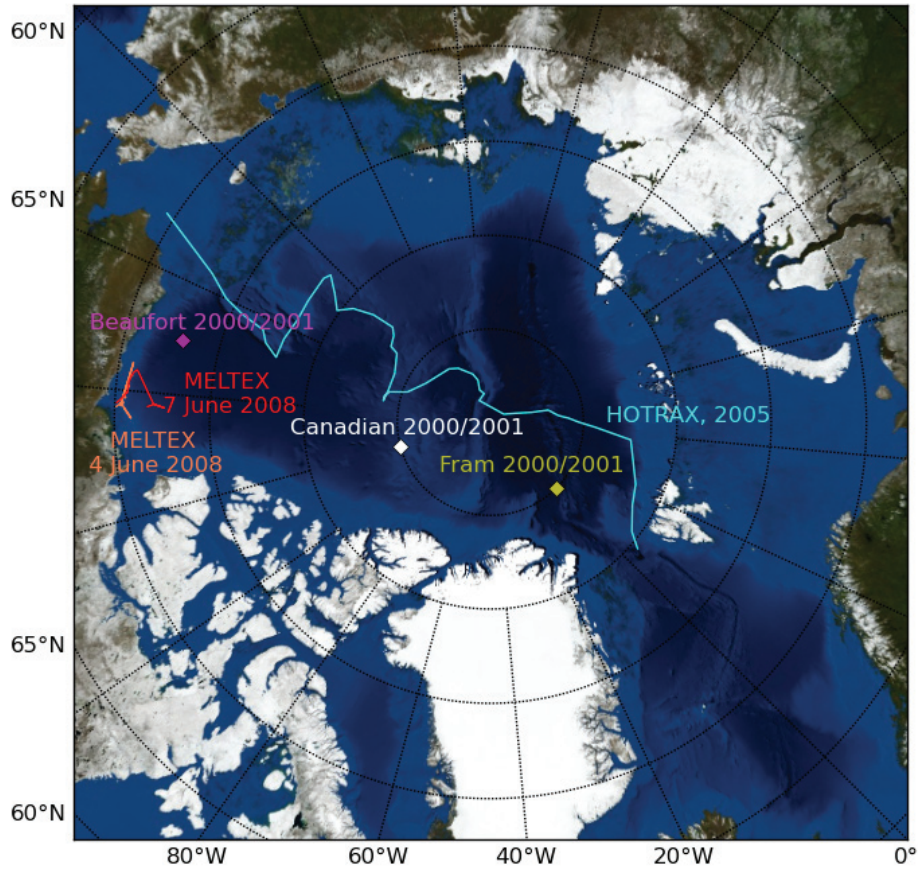

Fig. 1. Tracks, locations and dates of used validation data sets. Detailed descriptions are given in the text.

TCD
5, 2991–3024, 2011

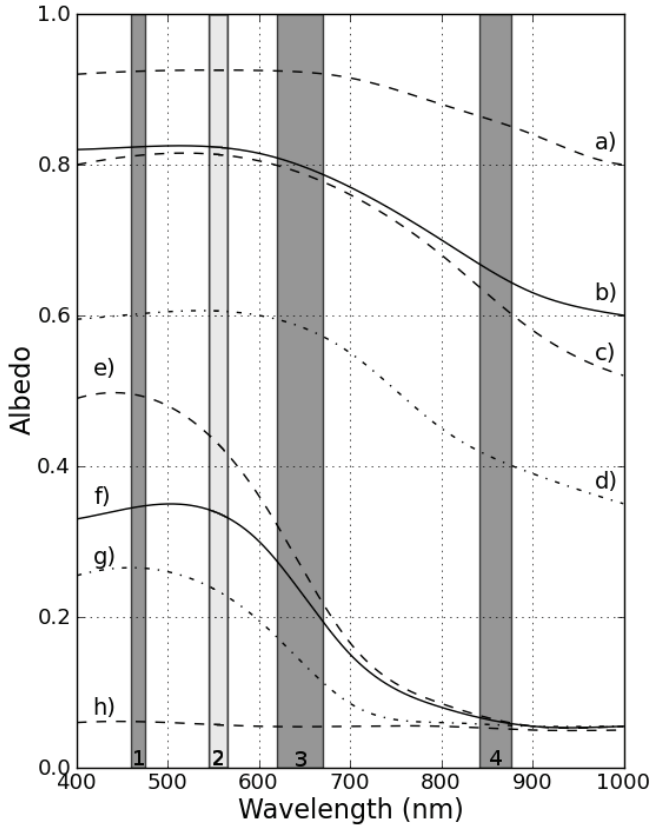

Fig. 2. Spectral albedo values for different surface types on Arctic sea ice: **(a)** Snow-covered ice (dry snow), **(b)** cold bare ice, **(c)** wet snow, **(d)** melting first year ice, **(e)** young melt pond, **(f)** and **(g)** two types of mature melt ponds, and **(h)** open water. The gray columns represent the range of the first four MODIS bands. For our study we use the spectral bands 1, 3, and 4 (albedo values after Grenfell and Maykut, 1977).

TCD
5, 2991–3024, 2011

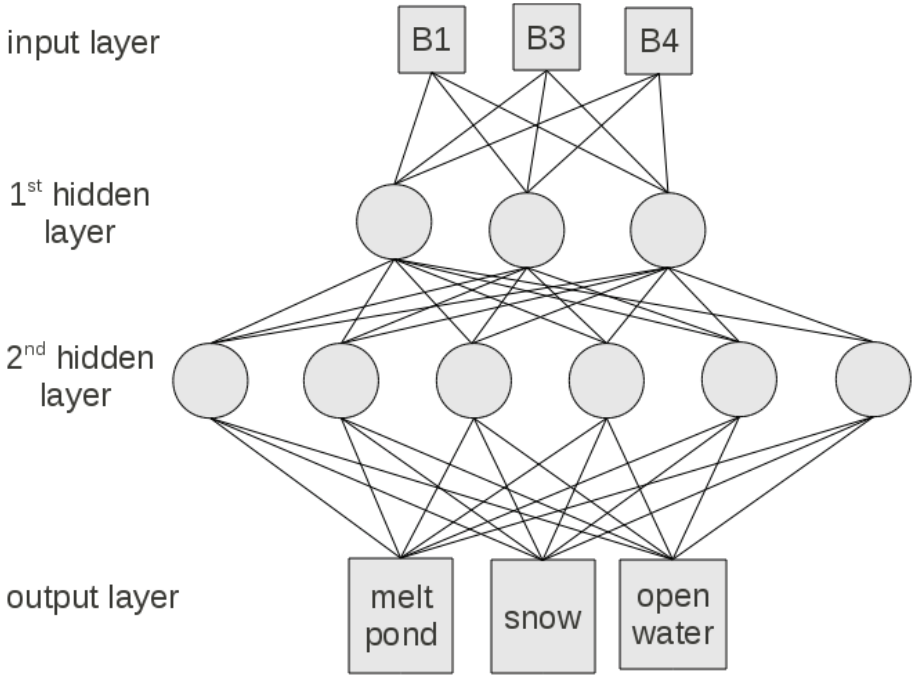

Fig. 3. Architecture of the MLP networks used for this study. The input layer are the MODIS surface reflectances for the three bands 1, 3, and 4. The hidden layers of the MLP used in our study contains 9 knots in the first layer and 27 knots in the second layer. For reasons of clarity this figure shows only 3 knots for the first and 6 knots for the second layer. The output layer contains the three classes melt pond, snow, and open water.

TCD
5, 2991–3024, 2011

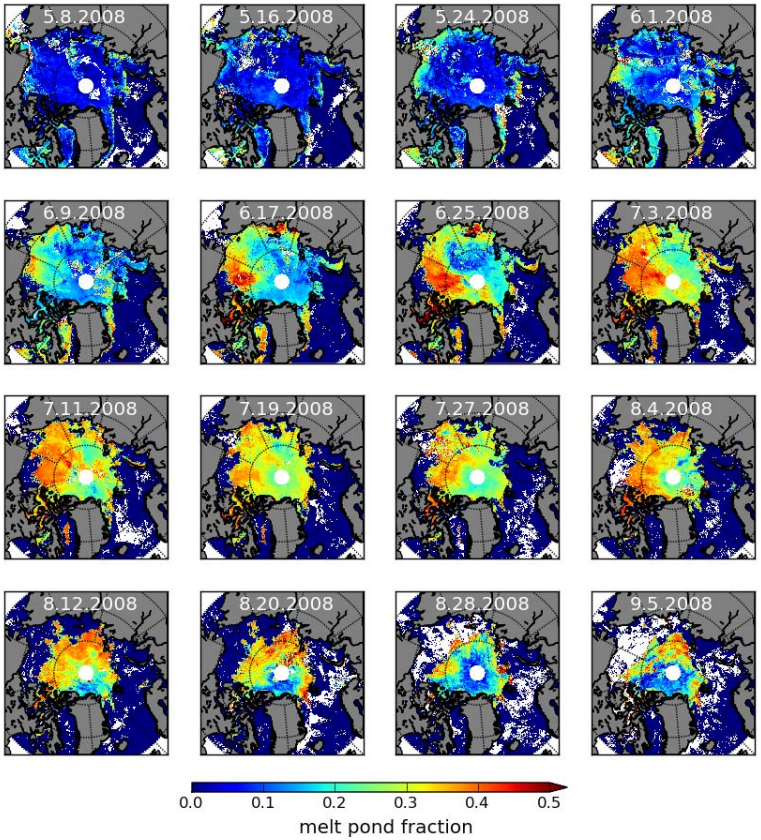

Fig. 4. Seasonal cycle of the melt pond fraction from MODIS satellite data for the Arctic, exemplary displayed for the year 2008.

TCD
5, 2991–3024, 2011

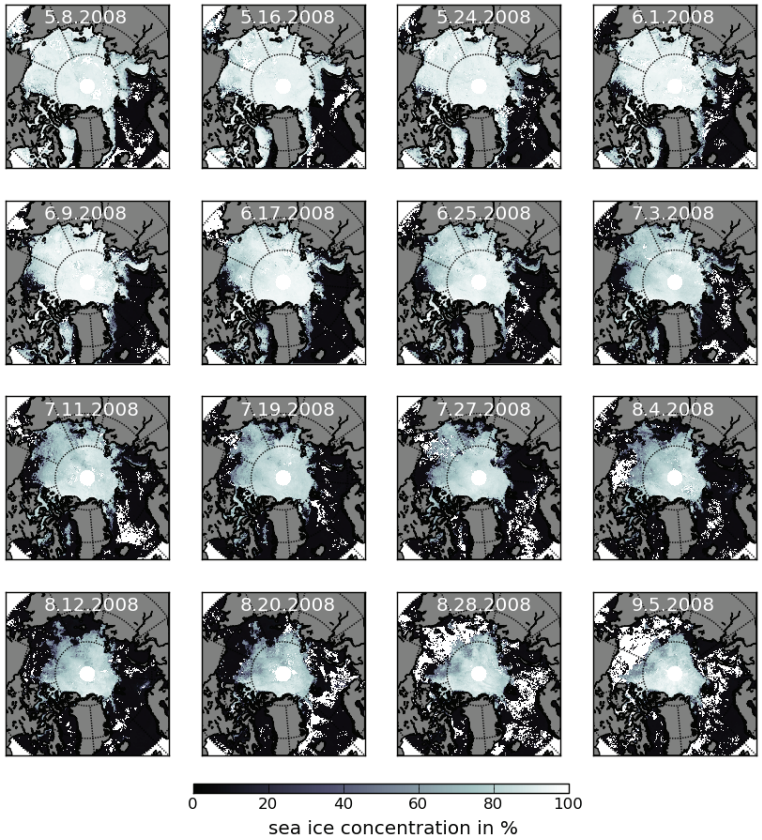

Fig. 5. Seasonal cycle of the sea ice concentration from MODIS satellite data for the Arctic, exemplary displayed for the year 2008.

TCD
5, 2991–3024, 2011

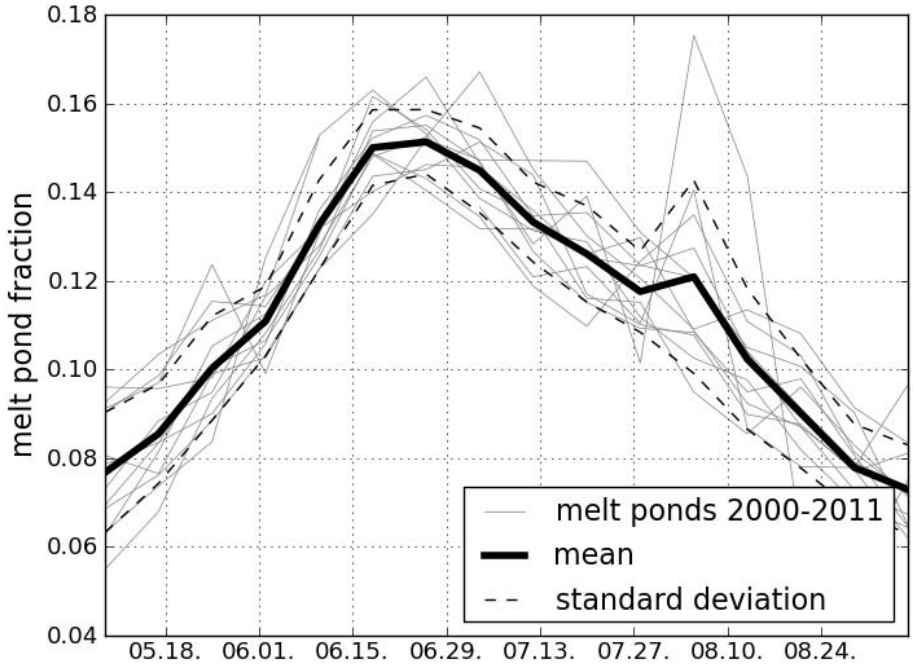

Fig. 6. Weekly mean melt pond fraction over the entire Arctic from 2000 to 2011. The light gray lines display the single years, the solid black line is the average over the last 12 yr. The dashed lines margin the standard deviation.

TCD
5, 2991–3024, 2011

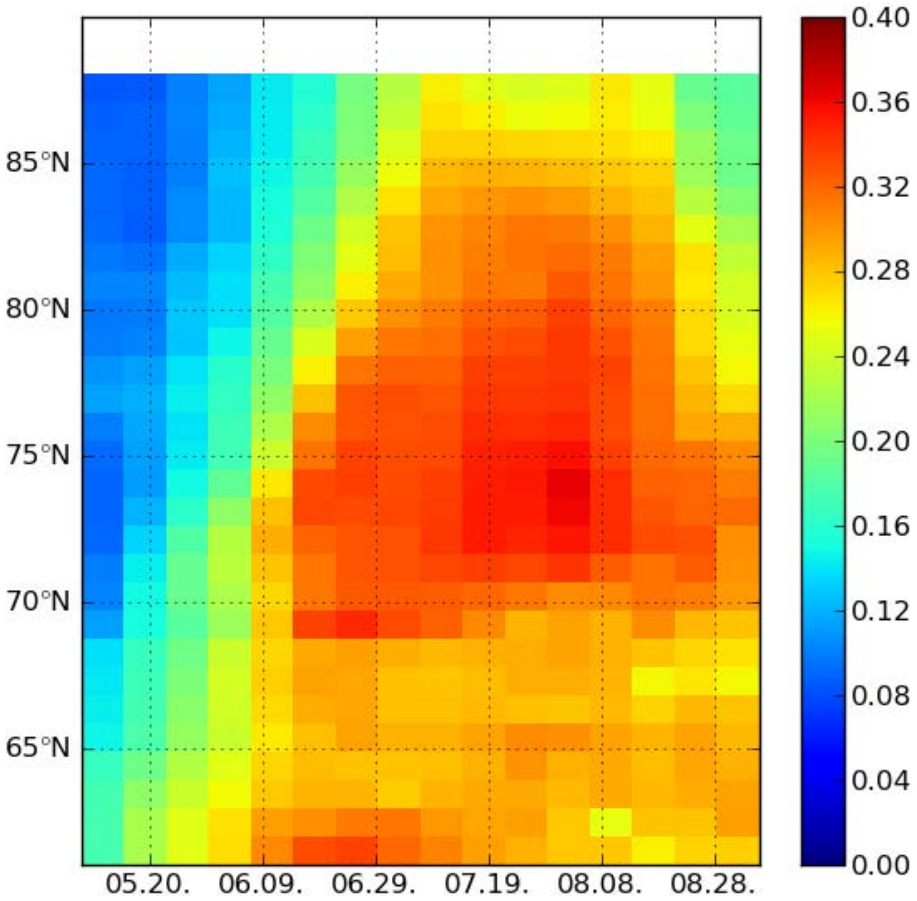

Fig. 7. Zonal mean melt pond fraction over the entire Arctic from 2000–2011.

TCD
5, 2991–3024, 2011

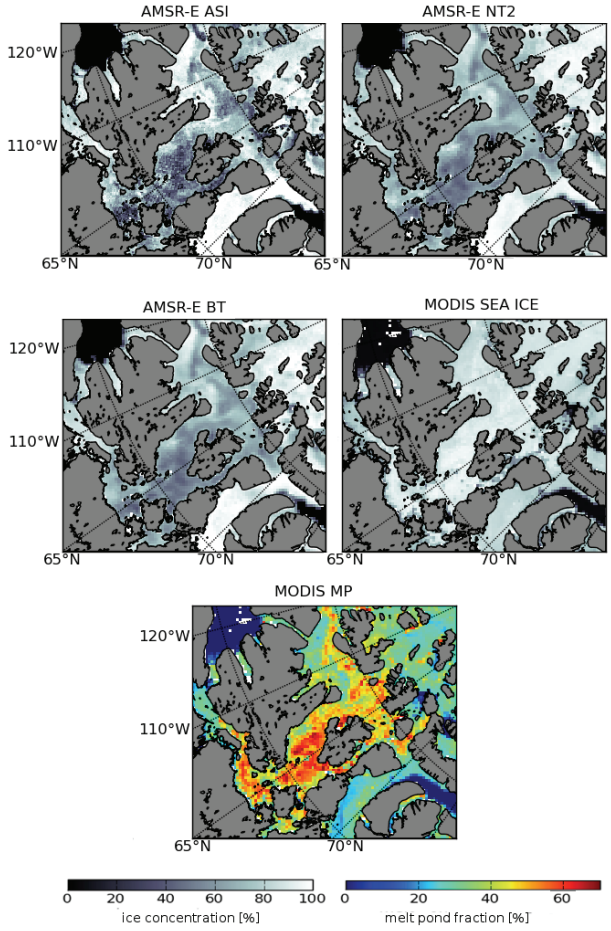

Fig. 8. Comparison of AMSR-E ASI (top left), AMSR-E NASA-Team 2 (top right), AMSR-E Bootstrap (middle left), and MODIS (middle right) sea ice concentrations. In the bottom MODIS melt pond fraction is displayed. All images are from 25 May 2008.

TCD
5, 2991–3024, 2011

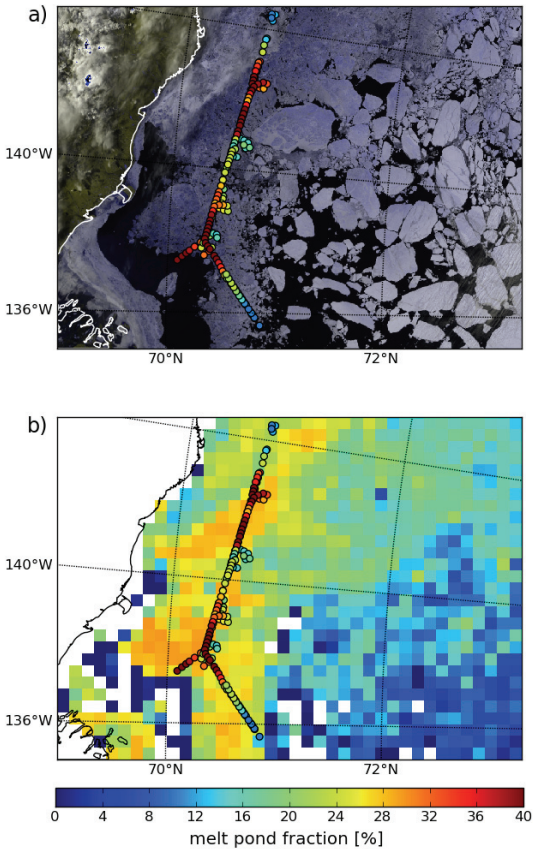

Fig. 9. (a) Spatial overlay of MELTEX melt pond results (dots) on a true color composite of MODIS level 1B data from 4 June 2008, 22:15 UTC. **(b)** MELTEX melt pond results (dots) from 4 June 2008 overlaid on MODIS melt pond fractions from mainly 5 June 2008 (detailed description in the text).

TCD
5, 2991–3024, 2011

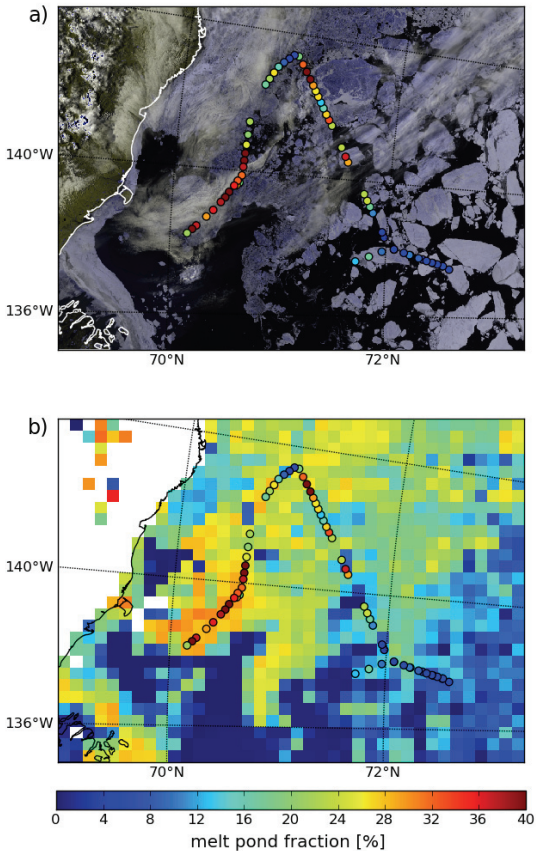

Fig. 10. **(a)** Spatial overlay of MELTEX melt pond results (dots) on a true color composite of MODIS level 1B data from 7 June 2008, 21:25 UTC. **(b)** MELTEX melt pond results (dots) from 7 June 2008 overlaid on MODIS melt pond fractions from mainly 7 June 2008 (detailed description in the text).

TCD
5, 2991–3024, 2011

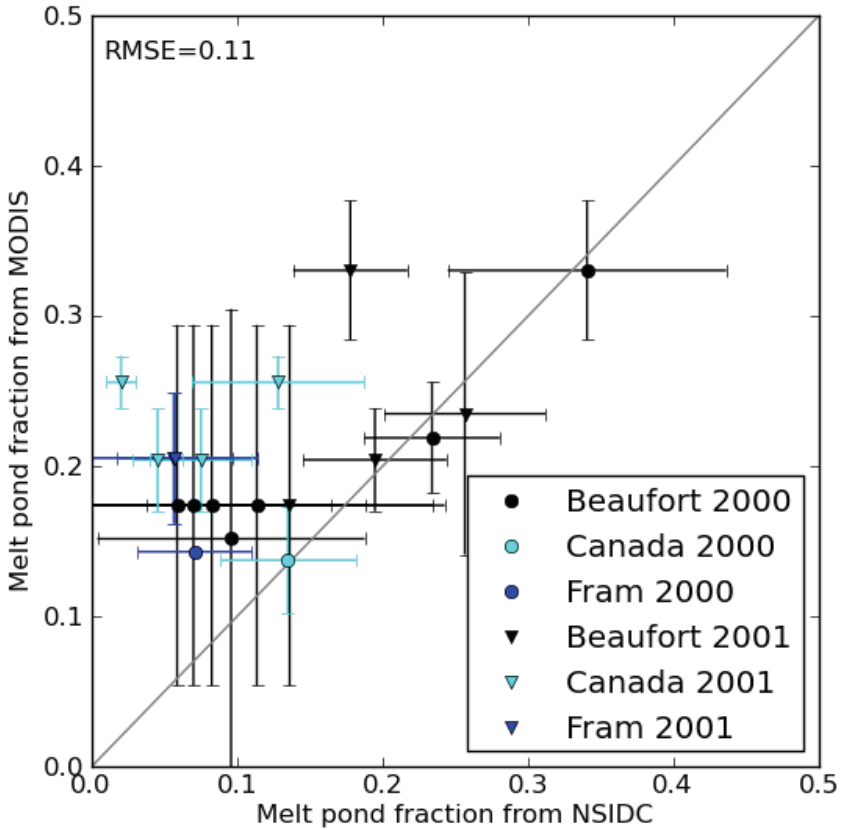

Fig. 11. Values from the MODIS melt pond product plotted versus NSIDC melt pond statistics for the years 2000 and 2001 and the three sites (i) Beaufort Sea, (ii) North of the Canadian Archipelago, (iii) and Fram Strait. The error bars are the standard deviation of the gridding from the results to $10 \times 10\,km^2$ for NSIDC data and to $12.5 \times 12.5\,km^2$ for the MODIS data. The RMSE is 10.7 % and the correlation $R^2 = 0.28$.

TCD
5, 2991–3024, 2011

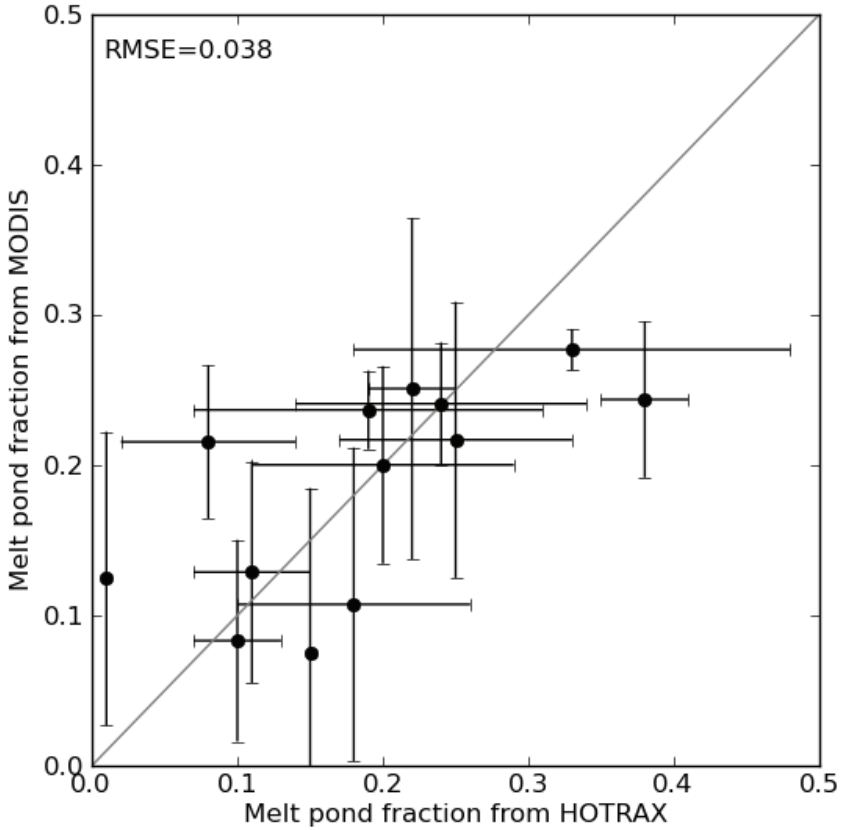

Fig. 12. Values from the MODIS melt pond product plotted versus ship observations from the HOTRAX cruise in 2005. The error bars are the standard deviation of the daily mean for the HOTRAX data and the gridding to $12.5 \times 12.5\,km^2$ for the MODIS data. The RMSE is 3.8 % and the correlation $R^2 = 0.45$.

TCD
5, 2991–3024, 2011